



A ray tracing method for predicting contrast in neutral atom beam imaging

S.M. Lambrick*, M. Bergin, A.P. Jardine, D.J. Ward

Department of Physics, The Cavendish Laboratory, University of Cambridge, Cambridge CB3 0HE, UK



ARTICLE INFO

Keywords:

Scanning helium microscopy
Atomic microscopy
Ray tracing
Simulated imaging
Helium atom scattering

ABSTRACT

A ray tracing method for predicting contrast in atom beam imaging is presented. Bespoke computational tools have been developed to simulate the classical trajectories of atoms through the key elements of an atom beam microscope, as described using a triangulated surface mesh, using a combination of MATLAB and C code. These tools enable simulated images to be constructed that are directly analogous to the experimental images formed in a real microscope. It is then possible to understand which mechanisms contribute to contrast in images, with only a small number of base assumptions about the physics of the instrument. In particular, a key benefit of ray tracing is that multiple scattering effects can be included, which cannot be incorporated easily in analytic integral models. The approach has been applied to model the sample environment of the Cambridge scanning helium microscope (SHeM), a recently developed neutral atom pinhole microscope. We describe two applications; (i) understanding contrast and shadowing in images; and (ii) investigation of changes in image formation with pinhole-to-sample working distance. More generally the method has a broad range of potential applications with similar instruments, including understanding imaging from different sample topographies, refinement of a particular microscope geometry to enhance specific forms of contrast, and relating scattered intensity distributions to experimental measurements.

1. Introduction

Neutral atom beam microscopy is an emerging technique that uses a focused or collimated beam of neutral atoms, principally helium, as a microprobe. The atom beam is typically fixed and the sample position is rastered. Atoms scattered in a particular direction are counted and used to build up a 2D micrograph, in a process similar to the operation of many other scanning microscopes. The method has considerable promise for non-destructive, exclusively surface sensitive, imaging of delicate samples within both the physical and biological sciences and for the formation of images with novel forms of contrast (Barr et al., 2016, 2014; Fahy et al., 2015; Koch et al., 2008). In helium images acquired to date, contrast appears to arise predominantly from variations in diffuse scattering due to the local surface structure ('topographic' contrast (Barr et al., 2016)) and is analogous to the established technique of secondary electron emission in SEM. However, at present there is no consistent method for predicting or understanding that contrast. With emerging evidence for chemical contrast (Barr et al., 2016) and the potential for diffractive and interference contrast, it becomes important to understand which features in images can be explained purely by diffuse scattering through sample topography.

Presented here is the development of a computational framework to construct topographic contrast in a scanning helium microscope

(SHeM) from a 3D model of the sample and signal collection environment. Ray tracing is used as the basis of our approach, treating helium atoms as classical rays that travel in straight lines. Compared to alternative techniques, such as wave propagation simulations, ray tracing is computationally inexpensive while still being able to capture phenomena such as multiple scattering. Multiple scattering is particularly important in neutral atom microscopy since helium atoms, unlike electrons or photons, are not absorbed or collected within the sample region. Beam atoms may therefore scatter multiple times from the sample and its surroundings, while still continuing to be detected. These multiple scattering processes can cause unexpected features in images, such as diffuse illumination (Witham and Sanchez, 2014); and could not be properly modelled using integral models (Hedgeland et al., 2005). Any integral model would have to be reformulated for each new geometry and would become computationally more expensive as the number of included scattering events increases, hence we consider them impractical for our needs. Ray tracing also allows the use of arbitrary sample geometries, thus it would be possible to use quantitative surface profileometry to generate the sample surface for simulation in future work. Quantum interactions with the sample are neglected, since it is known that the scattering of helium from all but the cleanest surfaces is largely diffuse (Engel, 1978; Poelsema et al., 1982).

The simulation framework was developed in house allowing

* Corresponding author.

E-mail addresses: sml59@cam.ac.uk (S.M. Lambrick), mb802@cam.ac.uk (M. Bergin), apj24@cam.ac.uk (A.P. Jardine), djw77@cam.ac.uk (D.J. Ward).

complete control of the scattering process, including defining the incoming helium beam profile, the sample geometry and the detection conditions. The source code is made available by the authors Lambrick (2018). Diffuse scattering was modelled using a specified angular distribution centered on the surface normal (typically a cosine distribution), enabling topographic contrast to be generated from an arbitrary sample profile. In principle, angular scattering distributions from the sample can be varied with spatial position, therefore enabling investigation into chemical effects. Rays scattered into a particular collection aperture were counted, enabling images to be constructed in exactly the same way as in the physical instrument. In addition the approach can be used to investigate instrumental factors such as the transmission of atoms through a particular detection geometry, and the consequence in images of the effusive beam components that have been seen in previous work (Fahy et al., 2015). The framework is currently optimised for the Cambridge SHeM, and can easily be adapted for similar atomic beam instruments.

The remaining paper is organised as follows. Section 2 discusses the Cambridge SHeM, ray tracing methods, and how these are related to the current work. Section 3 details the implementation of the simulation. Section 4 presents an illustrative comparison between experimental and simulated images, and explores the utility of the simulation for characterising collection aperture transmission probabilities in the SHeM. Finally, Section 5 gives a summary and outlook.

2. Background

2.1. Main SHeM components

Scanning helium microscopy uses a collimated thermal energy helium beam as a probe that is rastered over the surface of a sample, to create a spatially resolved image. Fig. 1 shows the main elements of a typical SHeM instrument; a more detailed description can be found in Barr et al. (2014). The helium beam is first produced by supersonic expansion of high pressure helium gas into a vacuum (Scoles, 1988). The centreline of the expansion is passed through a skimmer, then a pinhole collimates the beam to form the microprobe. Beam-widths of $\sim 1 \mu\text{m}$ (Eder et al., 2012) have already been demonstrated by using Fresnel zone-plates and there is a roadmap to achieve a usable resolution of $\sim 50 \text{ nm}$ in the next generation of SHeM. Similarly, a resolution of 350 nm has been reported by using very small working distances, 10–30 μm (Witham and Sanchez, 2012, 2011). Atoms within the microprobe are scattered by the sample, depending on the local beam-surface interaction. Images are then constructed by rastering the sample in the beam, while detecting the helium intensity passing through a detection aperture in a particular direction, using a custom high sensitivity helium detector (Alderwick et al., 2008). The ‘brightness’ of each pixel is proportional to the number of helium atoms detected while the sample is in a particular position.

For contrast prediction, the exact details of the source and detector need not be considered. The lower section of Fig. 1 shows an enlarged view of the sample region, containing the most important elements for the present simulation framework. These include the 90° total scattering geometry and 45° angle of incidence, the exact positioning of the pinhole and detector apertures, and the extent of the solid geometry surrounding the measurement area. Usually, the beam is incident on the sample at the point of co-incidence between the incoming beam and the outgoing detector cone.

2.2. Diffuse atom surface scattering

Unlike in charged matter microscopy, where there is significant penetration into the surface, thermal energy helium atoms scatter as a result of the repulsion between the valence electrons in the scattering atom and the valence electrons in the surface (Farias and Rieder, 1998). There is no penetration into the bulk, hence it is only necessary to

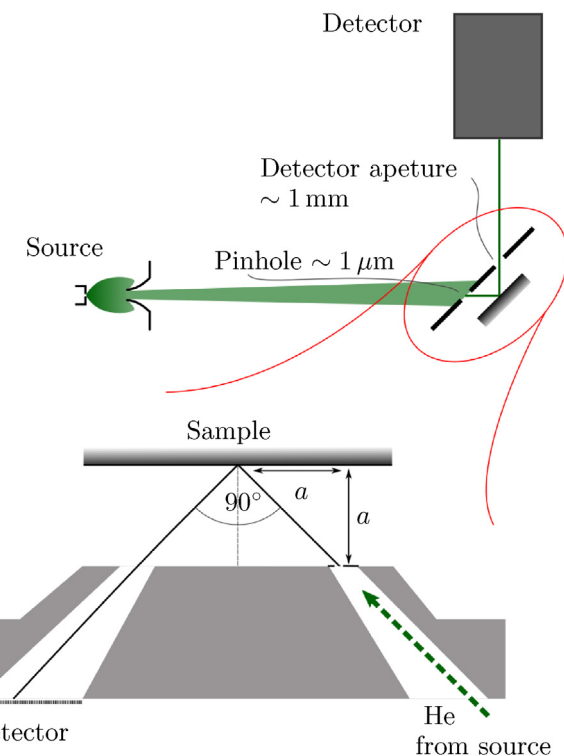


Fig. 1. Simplified schematic of a scanning helium microscope (SHeM), showing the principle of operation. The helium beam is formed in a supersonic expansion, then collimated by a skimmer and pinhole. Atoms scatter off the sample and those that enter the detector are counted. The image is formed by rastering the sample position. The close up shows the key parts of the instrument that are relevant to the current simulation framework, including the sample position and the mounting plate for both the pinhole and detector apertures. In the current Cambridge SHeM configuration $a \approx 2.1 \text{ mm}$.

define how atoms in the simulation respond to scattering from the topmost electronic surface of the sample. For scattered helium atoms the outgoing direction could be specular (Politano et al., 2011), a diffraction pattern (Traeger, 2006), involve rainbow effects (Miret-Artés and Pollak, 2012), or diffuse scattering (Poelsema et al., 1982).

Any randomness of the surface on a length scale between the wavelength of the atoms and the beam width (which spans 4 orders of magnitude) will have an effect on the observed scattering distribution, which is then averaged over the area of the beam. For scattering from such ‘rough’ surfaces, the averaged scattered direction is expected to be independent of incident direction, and to correspond to a normally centred cosine distribution (Greenwood, 2002). Since we are focussing on the generalised ‘topographic contrast’ associated with most ‘real’ surfaces imaged using SHeM, the framework presented here uses that normally centred cosine distribution. The intensity scattered into an infinitesimal solid angle, $d\Omega$, in a particular direction defined by the polar angle to the surface normal, θ , and the azimuthal angle, φ , is given by

$$I(\theta, \varphi) d\theta d\varphi = \frac{\cos \theta d\Omega}{\int_{2\pi} \cos \theta d\Omega}, \quad (1)$$

where the integral normalises the distribution over the outgoing half-space. Given that $d\Omega = \sin \theta d\theta d\varphi$, we can substitute and integrate to obtain the azimuthally independent result

$$I(\theta) = \frac{1}{\pi} \sin \theta \cos \theta. \quad (2)$$

Note that the cosine scattering distribution is independent of incident direction. Fig. 2 shows the cosine distribution of scattered atoms, and indicates the selection of some of those atoms by a detector cone to

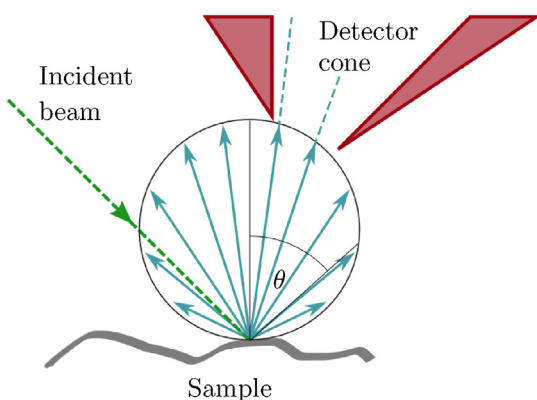


Fig. 2. Schematic showing the origin of topographic contrast by diffuse scattering. Incoming atoms are scattered in all directions by a surface-normal cosine distribution (shown here is a 2D distribution). A subset of those scattered atoms are selected by the detection cone, and used to determine the subsequent pixel brightness.

form contrast. In principle, any distribution can be incorporated into the present framework, and thus there is the opportunity to use SHem imaging to examine different distributions, e.g. $\cos^n(\theta)$ distributions, distributions with a specular bias, or diffraction patterns. Deviation of experimental data from simulated images generated using the present model would suggest non-diffuse scattering.

2.3. Ray tracing

Ray optics can model the propagation of waves as lines provided that changes in the medium that the waves travel through are on a much longer length-scale than the wavelength of the waves. It has been used extensively in physics to model electromagnetic (Born and Wolf, 1968) and seismic waves (Dahlen and Tromp, 1998), among others. Ray tracing is the numerical implementation of ray optics. As well as its use in science, ray tracing has been used extensively in the production of high quality photo-realistic computer graphics. Ray tracing calculations, can however, become complex in media where wave propagation is non-linear. In the present study propagation of helium atoms through vacuum is linear, so a large number of rays can be computed in relatively short amounts of time.

3. Simulation method

3.1. Principles

We limit our analysis to start at the collimating pinhole and to end at the back of the detector cone in the ‘pinhole plate’, as shown in Fig. 1. It is essential to include the full geometry of the mounting for the pinhole and detector apertures, as atoms may scatter multiple times between the sample and the plate. Atoms are considered to be ‘detected’ if they reach the surface at the rear of the detector cone. As a pinhole is used rather than a focussing element there is no true focal plane for the instrument,¹ although the beam broadens linearly with distance beyond the pinhole, depending on the position and size of the helium source. To simplify the present model, we consider a parallel beam with a two-dimensional Gaussian density profile whose full-width-half-maximum (FWHM) can be adjusted as required. In the results presented later we use a FWHM of $3.5\text{ }\mu\text{m}$ to match the beam-width associated with the experimental images, as measured by scanning over knife edges. A Gaussian profile was chosen for the representation of the beam as it provides an easily implemented model with a single free parameter.

The mathematics of the Gaussian distribution also allow for the combining of different beam broadening effects. In the present work the exact profile of the beam is unimportant, however in future work one could use more accurate trigonometric models of atomic beams that have been used with some success (Scoles, 1988).

In addition to the direct supersonic beam through the pinhole, background gas in the differential pumping region between the skimmer and pinhole can lead to an additional, broad, effusive beam through the pinhole (Fahy et al., 2015). We include a diffuse component in our simulation framework to reproduce this effect. As the mean free path of the helium atoms is much larger than the size of the pinhole, the effusive beam will follow a cosine distribution centred on the pinhole normal. The relative contributions of the collimated and effusive beams can be adjusted as required. Current experimental limitations mean we do not accurately know the pressure behind the pinhole hence we are prevented from predicting the flux of the effusive beam, thus a rough comparison between experimental and simulated images was used. The comparison suggests the effusive flux is comparable to, or larger than, the direct beam. In the present work the flux of the effusive beam was the same as the flux of the direct beam.

The surfaces of solid objects can be represented for ray tracing using analytic forms (Spencer and Murty, 1962). Here, we model all surfaces as triangulated meshes, which can represent arbitrary shapes. Such a mesh consists of a list of points in space and information on which points join together to form triangles. While triangulation can represent polyhedra of any complexity perfectly, one limitation is that it can only represent an approximation to curved surfaces, although the general method presented could be used with a different surface representation.

The ray tracing method used follows that described in “*The Fundamentals of Computer Graphics*” by Marschner and Shirley (2016). Rays have a position and a direction, and in each ray propagation step the nearest intersection of the ray with a triangle is found. After the location of the intersection is found, the position of the ray is updated and its direction is replaced, as desired. As part of the procedure it is possible to store the number of times a particular ray has hit an object and the distance it has travelled.

Rays are constructed at the location of the pinhole according to defined distributions for position and direction—specifically the Gaussian direct beam and the cosine effusive beam. Fig. 3 shows the four possibilities for a traced ray. First, the ray may intersect another surface and we simply repeat the procedure, i.e. it may ‘continue’. Second, the ray may not hit any surface and pass beyond the simulation volume—we describe it as having ‘left’ the simulation, and the ray is considered not to have been detected. Third, the ray may hit the detector surface, in which case we terminate its propagation and count it as ‘detected’. Finally, after a certain number of scattering events or a certain distance travelled, the ray may be artificially stopped which we describe as ‘discarded’. As such, the simulation acts to generate data on a single pixel at a time, and the number of detected, left, and discarded rays is collated. 1D and 2D images are constructed by rastering the sample, directly analogously to the operation of the experimental instrument, and using the number of detected rays for each position to form a simulated image.

3.2. Implementation

The core ray tracing is performed in C to optimise performance. Around the core is a MATLAB wrapper that prepares all the parameters and analyses data, MEX is used to call the core computation directly from within MATLAB. Sample and pinhole plate geometries are imported into MATLAB as binary stereolithography (.stl) files, which can be created by CAD software. AutoDesl Inventor and FreeCAD were used in the current study. The triangulation of surfaces is performed by the CAD package during the export to .stl process.

Rays are generated according to the desired distributions in MATLAB, and geometries are manipulated as needed. The ray tracing

¹ Other instrument factors, such as the solid angle of the detector aperture, limit the range of working distances that can be used effectively.

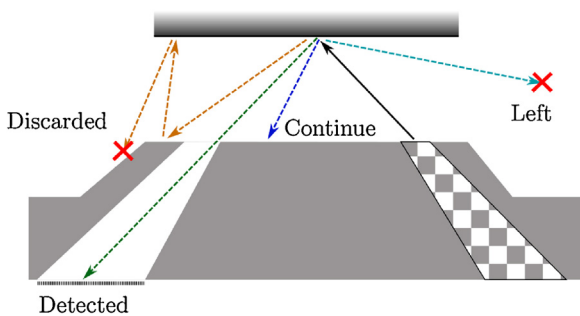


Fig. 3. The four possibilities at each iteration of a ray being traced. Normally, the ray will ‘continue’ to its next iteration, but can also be ‘detected’ when it hits a suitable surface, can be treated as having ‘left’ the simulation volume, or can be ‘discarded’ if it exceeds a certain number of steps or trajectory length. The incoming cone (marked in checkerboard pattern) is not included in the simulation.

for each pixel is performed in the core function, with the wrapper rastering the sample between each pixel. As each pixel is independent parallelization can be implemented, considerably speeding up the computation and making the use of high performance computing practical.

1D line scans and simple 2D images may be performed using the method on a desktop computer. Computation time is linear with the number of triangles used to represent the surfaces, the number of pixels simulated and the number of rays used per pixel. A line scan using 451 pixels and 8×10^7 total rays per pixel for a geometry containing 336 triangles takes 37 min on an Intel Core2 quad processor clocking at 2 GHz.

4. Results and discussion

4.1. Imaging of a standardised tick mark

SHeM images have been taken of a standardised tick mark within a TEM grid (G2000HA Fine Hexagonal Mesh from Gilder Grids Ltd.), mounted on an adhesive carbon tape. For comparison an optical microscopy image is shown in Fig. 4, where the copper grid can be seen on top of the black tape. The grid is 12.5 μm thick; the tick mark is punched all the way through the grid and is rectangular in cross section. The tick mark has a well defined geometry, so was selected as an

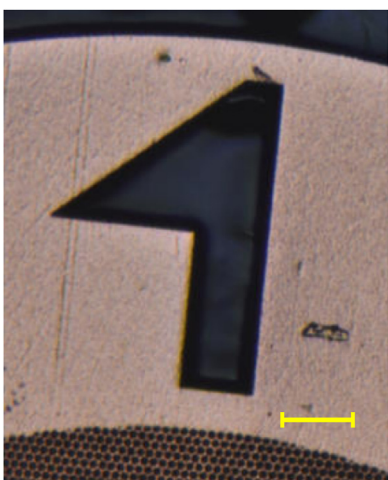


Fig. 4. An optical micrograph of the standardised tick mark. The tick mark is a hole all the way through the metal of the 12.5 μm thick grid. The copper grid can clearly be seen on the black carbon tape. It can also be seen that the tape inside the tick mark is not entirely flat. The scale bar is 100 μm.

idealised 3D geometry with which to compare the simulation results.

Fig. 5 shows a comparison between an experimental SHeM image of the tick mark (left) and a simulated image (right), as well as the orientation of the incoming and detected beams (top). Unlike in the optical image, in the SHeM micrograph there is not a clear distinction between the copper and carbon tape, which is most likely due to the helium image providing exclusively topographic information. On the left hand side of the tick are areas of lower intensity, labelled (1), and on the right there are bright regions, labelled (2). The lower intensity features have previously been attributed to shadowing and masking (Barr et al., 2016), where the direct line of sight from the point where the incident beam hits the surface to the detector, is blocked, as shown in Fig. 6(a). Similarly, the bright regions may be due to diffuse illumination, a multiple scattering effect where atoms hit a second surface within the sample and are then scattered into the detector, as shown in Fig. 6(b). However, previously it has not been possible to explicitly confirm these suggestions.

Masking and diffuse illumination are both implicitly included in our simulation framework, enabling us to test these mechanisms. The simulated image in Fig. 5, does indeed show both of these major features. In addition, small masks are predicted along the lower horizontal edges of the tick mark, although it should be noted that these edges are angled slightly away from horizontal. Similar weak masks are present in the experimental image. Feature (3) is a larger mask relating to the carbon tape separating from the grid, creating a larger mask. The upper tick edges are oriented away from horizontal in the opposite direction. Here, feature (4), diffuse illumination is predicted.

By counting the number of times rays scatter from the sample it is possible to decompose the image into contributions from single and multiple scattering. Such a decomposition is shown for the same tick mark in the left and middle images of Fig. 7. It can clearly be seen that the diffuse illumination around the stepped edges of the feature is associated with multiple scattering, and that masks result from the single scattering detection path being blocked. We can therefore unambiguously conclude that these edge features are a result of masking and diffuse illumination due to surface topography and measurement geometry. In the simulated image the ratio of the variation between the single scattering counts and the variation of the multiple scattering counts implies that multiple scattering accounts for approximately 20% of contrast, though this will vary from image to image.

Fig. 7 also shows the image (right) associated with atoms from the effusive component of the beam. It is clear that the effusive beam acts only to add a background and associated shot noise to the image, since at a working distance of ~1 mm the effusive beam is very large compared to the image size it therefore provides no spatial resolution. On scales comparable to that of the sample mounting the effusive beam adds a slowly varying background, as does multiple scattering between the sample and the pinhole plate.

All simulated images had black assigned to the pixel with the fewest detector counts and white assigned to the pixel with the most. Simulated images were created with 1 μm pixels and 137,832 rays per pixel. The effusive beam was modelled with the same number of rays as the direct beam. The average contribution of the effusive beam to the total signal was 20%.

4.2. An improved tick mark topography

It can be seen in Fig. 5 that there is one significant deviation between the experimental and simulated images—the size of the mask on the left hand side of the tick mark, feature (1). Given the depth of the grid and the 45° geometry it would be expected that such masks would appear ~25 μm in width in the helium image. The simulation reproduces the expected size, but in the experimental image the mask features are much smaller. The most likely explanation is that the simplified topology used in the simulation must differ from that of the experimental sample.

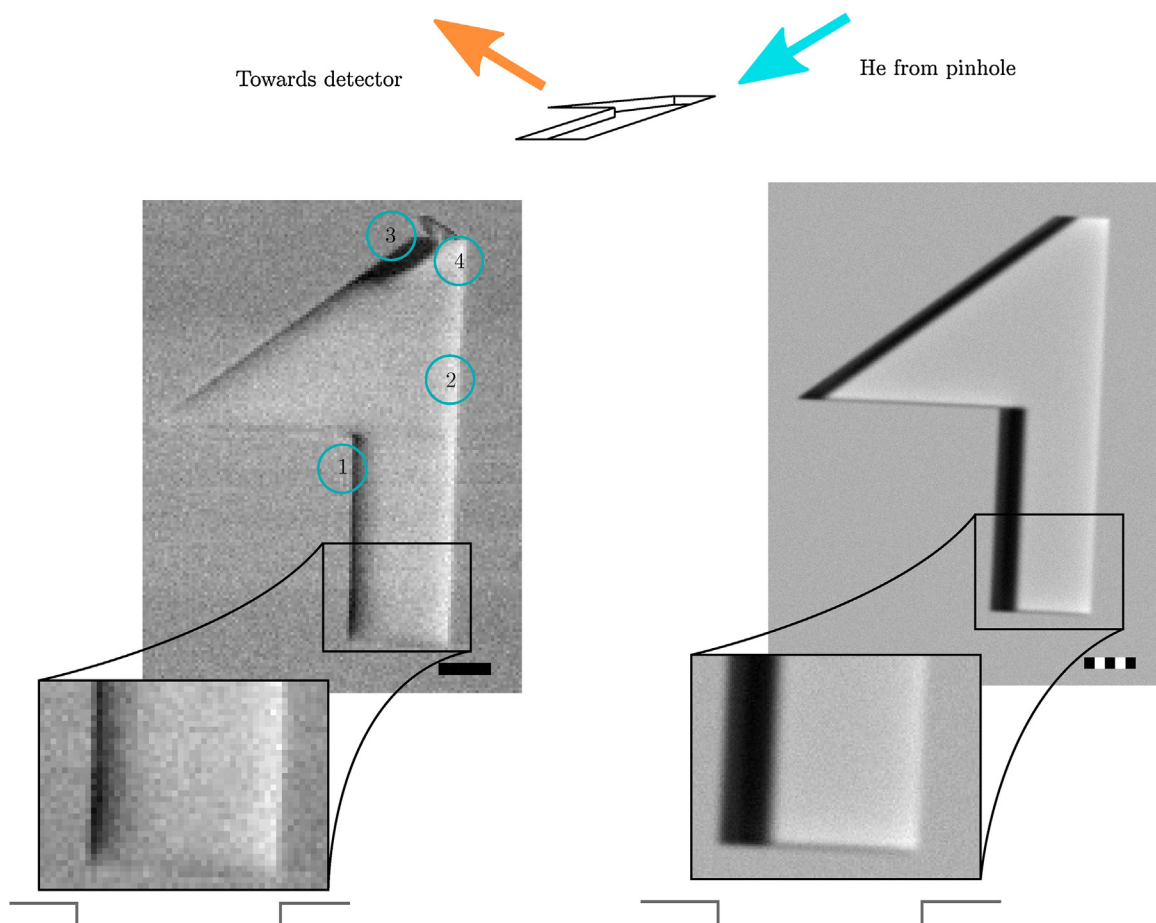


Fig. 5. Comparison between experimental (left) and simulated (right) SHeM images of a TEM grid tick mark. The grid is 12.5 μm thick, mounted on adhesive carbon tape. The orientation of the incoming and outgoing helium beams is shown at the top. The topography is shown below the close up sections of the image. Both scale bars are 50 μm . Feature 1 is a result of masking and feature 2 is due to diffuse illumination. The dark region at the top of the experimental image, feature 3, is a result of the carbon tape bending away from the grid, as can be seen in the optical image, resulting in a larger mask. Feature 4 shows diffuse illumination at the top of the tick mark.

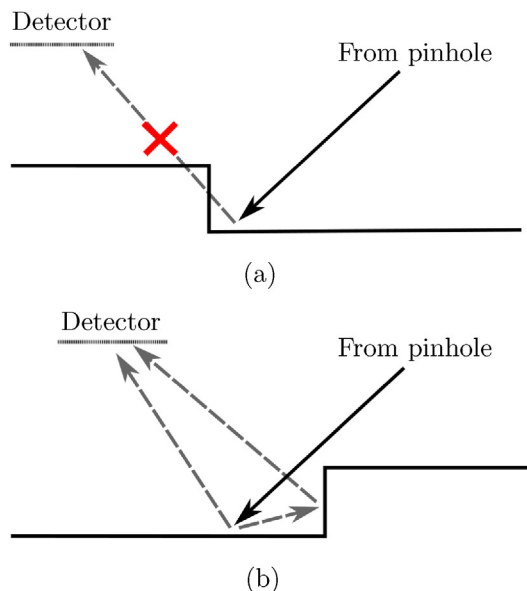


Fig. 6. Illustration of features arising as a result of topographic contrast. (a) Masking occurs when atoms scattered from the direct beam cannot enter the detector directly due to a topographical feature blocking the line of sight. (b) Diffuse illumination arises from large features near the point of incidence of the incident beam, potentially amplifying the detected signal.

In the optical image it appears that the carbon tape inside the tick mark is bending, though it is not entirely clear in what manner. In order to examine the differences between the experimental and simulated results, several different models for the interior region of the tick mark have been studied. Several examples are compared with the experimental data in Fig. 8. Using the same simulation, a model that includes a raised interior showed reduced masking, as in Fig. 8(a). However, the masking at the bottom of the tick mark and the diffuse illumination on the right hand side is also removed. An improved result can be obtained by making the profile steeper, as in Fig. 8(b), which maintains the diffuse illumination on the right hand side, although the light region at the bottom of the image also persists. The most similar image to the experiment were obtained with a sharp rise at the edges, followed by a more gradual bending over the interior, as in Fig. 8(c). Such a topography can be explained by both bending of the tape, as seen in the optical image, and deformation of the tape below the copper of the grid, thus making the topographic height difference between the grid and tape less than was initially assumed. Thus we see that topographic information is encoded into the helium image that is not clearly evident in the optical image.

Quantitative profilometers, such as AFM, STM or stylus profilers, could have been used to find the true surface profile across the tick mark. However, the aspect ratio issues of such devices would have to be addressed, for example using specialist AFM tips (Chen et al., 2006), as large sharp features exist in the sample used. In the current study, which is principally motivated by the simulation method, such data was

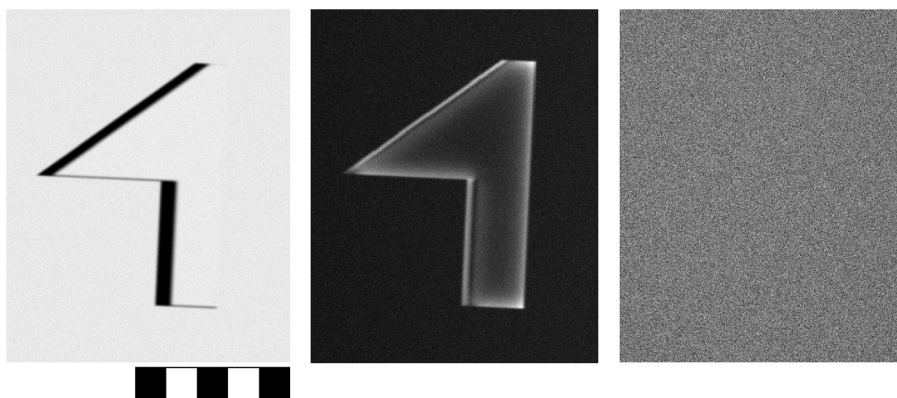


Fig. 7. A simulated image of the tick mark, separating different contributions: single scattering (left), multiple scattering (middle), and effusive contribution (right). The scale bar is 250 μm . Here the origins of the two contrast features can be confirmed. It should be noted that the multiple scattering contribution to contrast is less, $\approx 20\%$ of the total, than the single scattering contribution. Despite being a smaller contribution multiple scattering features are observable in both the total simulated image and the experimental image—[Fig. 5](#).

not taken. For future studies on helium contrast such information would be highly valuable.

4.3. Analysis of transmission probabilities

In addition to using the simulation to model and understand experimental images, it is possible to use simulated results to characterise the response of the instrument and thus to understand potential improvements. To illustrate use of the simulation framework in this respect, we examine the effect of sample position for a given detection geometry. The topographic contrast formed in a SHeM is dependent on the shape of the ‘detector cone’ shown in [Fig. 1](#). Atoms scattered by the sample must pass through the cone to reach the helium detector. The response of the instrument is therefore dependent on the transmission of atoms through the cone, which in turn depends on the angle with which scattered atoms enter the region. Here, the present simulations are used to obtain a quantitative relationship between the transmission probability and sample position.

Since the sample is scanned laterally, it is only relevant to examine how transmission varies with perpendicular distance from the standard working point (at the intersection of the incoming beam and detector cone axes). We simulate a flat sample that is moved backwards diagonally, as shown in [Fig. 9](#). To examine the effects of the cone transmission probability separately from the sample scattering distribution, a uniform scattering distribution was used. In a similar manner to the derivation of equation [\(2\)](#), and using the same notation, we can reach an azimuthally independent intensity distribution

$$I(\theta, \varphi) = \frac{d\Omega}{\int_{2\pi} d\Omega} \quad (3)$$

$$I(\theta) = \frac{1}{2\pi} \sin \theta. \quad (4)$$

As the sample is moved back, the solid angle of the detector entrance aperture also changes, as shown schematically in [Fig. 9](#) and plotted with distance in [Fig. 10](#). The simulation results were then normalised by this variation in solid angle, to give a measure of the transmission probability only.

[Fig. 10](#) shows as solid line the relative transmission probabilities of the detector cone, as a function of the perpendicular distance the sample is placed from the standard working point. We find the function is strongly peaked, indicating that there is a strong change in transmission probability as the sample position is varied, which is not a result of the solid angle of the detector aperture changing. The distribution has several consequences. Firstly, it means the SHeM has an effective depth of field related to the signal transmitted, in addition to the effects of the detection solid angle. Images can still be successfully taken outside of the range, but there is a substantial drop in signal that renders such images noisy. Secondly, the peaked shape of the response will result in an inversion of the contrast formed by large scale sample

height differences, depending on whether imaging is performed with the sample closer or further than the standard working position. If one were interested primarily in working distance contrast, arising from the effects of transmission probability and solid angle variations, it would be prudent to image on the steep slope just off the peak of the curve in [Fig. 10](#). It should, however, be noted that other contrast mechanisms, such as the local angle to the surface, as well as masking and diffuse illumination, are manifest at all working distances. For microscopic samples, working distance contrast is over distances much larger than the usual sample size. Working distance contrast applies over distance of $\sim 100 \mu\text{m}$ or larger with the current levels of signal to noise routinely achieved ([Fahy et al., 2018](#)).

After the detector cone there are further components through which atoms must pass before reaching the detector itself. To examine whether the transmission through these additional components is affected by the direction or position of atoms entering the detector cone, a MolFlow+ ([Kersevan and Ady, 2017](#)) simulation was used to calculate the transmission probability of all components from the sample to the detector, also as a function of sample position. A uniform source of gas was used in the MolFlow simulation, moved backwards in the same manner as the sample in the SHeM simulation. The results, normalised by the solid angle of the entrance aperture, are shown as points in [Fig. 10](#) and demonstrate a very high level of agreement with our ray-tracing framework. The agreement demonstrates that transmission through the components beyond the detector cone are not affected by the distribution of atoms entering the cone. Overall, these results demonstrate that the geometry of detector apertures and detector cones can play a significant role in contrast in SHeM images, and that in the current setup of the Cambridge SHeM no further components need to be considered in this respect.

5. Conclusions and summary

A ray-tracing method for producing simulated atom beam images from a three dimensional model of sample topography was presented. A series of simulated SHeM images produced were shown to be in close qualitative agreement with experimental results. The utility of the method was shown in understanding how subtle topological features, such as the behaviour of the carbon tape, can result in significant differences in helium atom images. Further, the potential to use such methods for investigating the experimental instruments themselves was demonstrated. The results makes clear the importance careful design of detector apertures and provide information about the effective depth of field in a SHeM. More generally, we envisage our simulation framework to be of considerable value in understanding future images, designing new equipment, and thus the overall development of the SHeM field.

Acknowledgements

The work was supported by EPSRC grant EP/R008272/1. S. M. L.

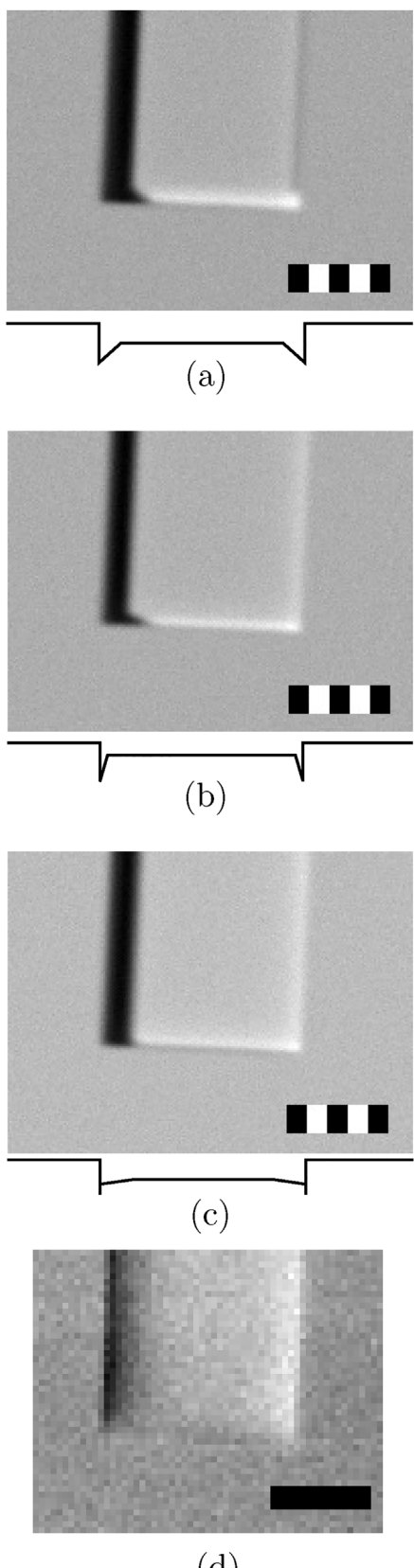


Fig. 8. Comparison of several different models for the interior region of the tick mark. (a–c) show simulated images with profiles as shown, compared to (d) the experimental image. The scale bar in each case is 50 μm .

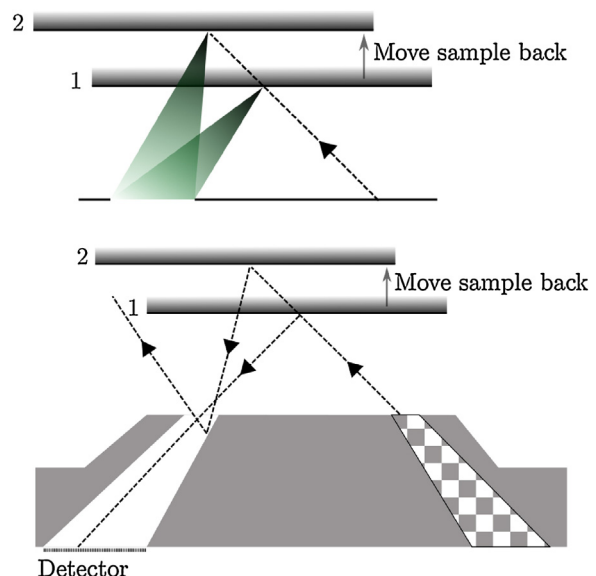


Fig. 9. As a sample is moved backwards, the angle that scattered atoms enter the detector cone changes, as does the solid angle subtended by the detector aperture. It can be seen that when atoms enter the cone at directions far away from parallel to the centre line of the cone, there is an increased chance of them leaving again through the entrance aperture.

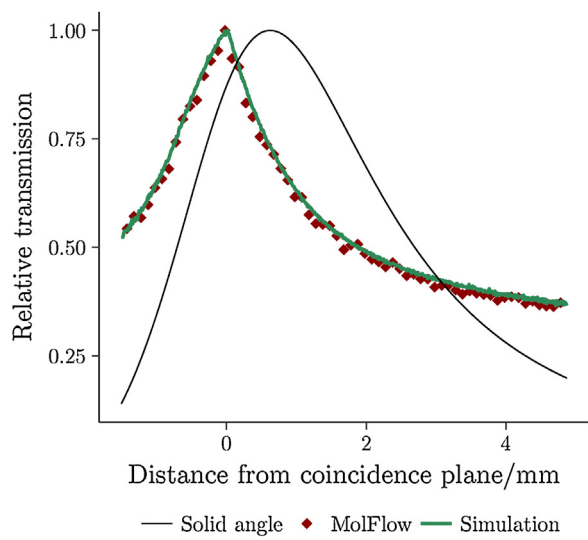


Fig. 10. Solid angle of the detector aperture, MolFlow + calculation for the complete sample and detector geometry normalised by the solid angle of the entrance aperture, and relative transmission probability of the detection cone. The three sets of data have been normalised to the maximum value of each data set. The maximum value of the solid angle is 0.094sr.

acknowledges funding from Mathworks Ltd. and M. B. acknowledges an EPSRC studentship. The authors would like to thank Dr. W. Allison and Dr. D. MacLaren for several useful discussions.

References

- Alderwick, A.R., Jardine, A.P., Hedgeland, H., MacLaren, D.A., Allison, W., Ellis, J., 2008. Simulation and analysis of solenoidal ion sources. *Rev. Sci. Instrum.* 79, 123301.
- Barr, M., Fahy, A., Jardine, A., Ellis, J., Ward, D., MacLaren, D., Allison, W., Dastoor, P., 2014. A design for a pinhole scanning helium microscope. *Nucl. Instrum. Methods Phys. Res. Sect. B: Beam Interact. Mater. Atoms* 340, 76–80.
- Barr, M., Fahy, A., Martens, J., Jardine, A.P., Ward, D.J., Ellis, J., Allison, W., Dastoor, P.C., 2016. Unlocking new contrast in a scanning helium microscope. *Nat. Commun.* 7, 10189.
- Born, M., Wolf, E., 1968. *Principles of Optics*, 4th ed. Oxford University Press.

- Chen, I.-C., Chen, L.-H., Orme, C., Quist, A., Lal, R., Jin, S., 2006. Fabrication of high-aspect-ratio carbon nancone probes by electron beam induced deposition patterning. *Nanotechnology* 17, 4322.
- Dahlen, F., Tromp, J., 1998. *Theoretical Global Seismology*. Princeton University Press.
- Eder, S.D., Reisinger, T., Greve, M.M., Bracco, G., Holst, B., 2012. Focusing of a neutral helium beam below one micron. *N. J. Phys.* 14, 073014.
- Engel, T., 1978. A molecular beam investigation of He, CO, and O₂ scattering from Pd (111). *J. Chem. Phys.* 122, 373–385.
- Fahy, A., Barr, M., Martens, J., Dastoor, P.C., 2015. A highly contrasting scanning helium microscope. *Rev. Sci. Instrum.* 86, 023704.
- Fahy, A., Eder, S., Barr, M., Martens, J., Myles, T., Dastoor, P., 2018. Image formation in the scanning helium microscope. *Ultramicroscopy* 192, 7–13.
- Farias, D., Rieder, K.-H., 1998. Atomic beam diffraction from solid surfaces. *Rep. Prog. Phys.* 61, 1575.
- Greenwood, J., 2002. The correct and incorrect generation of a cosine distribution of scattered particles for Monte-Carlo modelling of vacuum systems. *Vacuum* 67, 217–222.
- Hedgeland, H., Jardine, A., Allison, W., Ellis, J., 2005. Anomalous attenuation at low temperatures in high-intensity helium beam sources. *Rev. Sci. Instrum.* 76.
- Kersevan, R., and Ady, M. 2017. Molflow+ is a Monte-Carlo code developed at CERN. URL: cern.ch/molflow.
- Koch, M., Rehbein, S., Schmahl, G., Reisinger, T., Bracco, G., Ernst, W.E., Holst, B., 2008. Imaging with neutral atoms—a new matter-wave microscope. *J. Microsc.* 229, 1–5.
- Lambrick, S. M. 2018. Shem ray tracing simulation v1.0.0. doi: 10.5281/zenodo.1228079.
- Marschner, S., Shirley, P., 2016. *Fundamentals of Computer Graphics*, 4th ed. Taylor and Francis.
- Miret-Artés, S., Pollak, E., 2012. Classical theory of atom–surface scattering: the rainbow effect. *Surf. Sci. Rep.* 67, 161–200.
- Poelsema, B., de Zwart, S.T., Comsa, G., 1982. Scattering cross section of low-coverage CO on Pt(111) for thermal He and H₂ beams. *Phys. Rev. Lett.* 49, 578–581.
- Politano, A., Borca, B., Minniti, M., Hinarejos, J.J., Vázquez de Parga, A.L., Farías, D., Miranda, R., 2011. Helium reflectivity and Debye temperature of graphene grown epitaxially on Ru(0001). *Phys. Rev. B* 84, 035450.
- Scoles, G., 1988. *Atomic and Molecular Beam Methods* /Edited by Giacinto Scoles. Oxford University Press, Oxford.
- Spencer, G.H., Murty, M.V.R.K., 1962. General ray-tracing procedure. *J. Opt. Soc. Am.* 52, 672–678.
- Traeger, F., 2006. Helium atom scattering from oxide surfaces. *ChemPhysChem* 7, 1006–1013.
- Witham, P., Sanchez, E.J., 2011. A simple approach to neutral atom Microscopy. *Rev. Sci. Instrum.* 82, 103705.
- Witham, P., Sanchez, E.J., 2014. Exploring neutral atom microscopy. *Cryst. Res. Technol.* 49, 690–698.
- Witham, P.J., Sanchez, E.J., 2012. Increased resolution in neutral atom microscopy. *J. Microsc.* 248, 223–227.